Available online at www.sciencedirect.com
ScienceDirect
International Journal of Multiphase Flow 34 (2008) 767–785
International Journal of Multiphase Flow
www.elsevier.com/locate/ijmulflow

Bubble and liquid turbulence characteristics of bubbly flow in a large diameter vertical pipe

M.E. Shawkat [a], C.Y. Ching [b,*], M. Shoukri [b]

[a] Fuel and Fuel Channel Safety Analysis, Nuclear Safety Solutions Ltd., 700 University Avenue, Toronto, Ontario, Canada M5G 1X6
[b] Department of Mechanical Engineering, McMaster University, 1280 Main Street West, Hamilton, Ontario, Canada L8S 4L7

Received 3 August 2007; received in revised form 11 January 2008

Abstract

The bubble and liquid turbulence characteristics of air–water bubbly flow in a 200 mm diameter vertical pipe was experimentally investigated. The bubble characteristics were measured using a dual optical probe, while the liquid-phase turbulence was measured using hot-film anemometry. Measurements were performed at six liquid superficial velocities in the range of 0.2–0.68 m/s and gas superficial velocity from 0.005 to 0.18 m/s, corresponding to an area average void fraction from 1.2% to 15.4%. At low void fraction flow, the radial void fraction distribution showed a wall peak which changed to a core peak profile as the void fraction was increased. The liquid average velocity and the turbulence intensities were less uniform in the core region of the pipe as the void fraction profile changed from a wall to a core peak. In general, there is an increase in the turbulence intensities when the bubbles are introduced into the flow. However, a turbulence suppression was observed close to the wall at high liquid superficial velocities for low void fractions up to about 1.6%. The net radial interfacial force on the bubbles was estimated from the momentum equations using the measured profiles. The radial migration of the bubbles in the core region of the pipe, which determines the shape of the void profile, was related to the balance between the turbulent dispersion and the lift forces. The ratio between these forces was characterized by a dimensionless group that includes the area averaged Eötvös number, slip ratio, and the ratio between the apparent added kinetic energy to the actual kinetic energy of the liquid. A non-dimensional map based on this dimensionless group and the force ratio is proposed to distinguish the conditions under which a wall or core peak void profile occurs in bubbly flows.

Keywords: Two phase; Bubbly flow; Large diameter; Pipe; Turbulence; Interfacial force; Bubble migration

1. Introduction

The local distribution of the bubble and the liquid turbulence characteristics such as the void fraction, bubble diameter, bubble velocity, liquid average and turbulent velocities in two-phase bubbly flow is important to understand the interaction between the phases. It is now well established that the scale of the pipe can have an effect on the flow patterns and phase distribution. Typically, for a vertical upward bubbly flow, when the diameter of the pipe (D_{pipe}) is greater than about 100 mm, the bubbles tend to migrate toward the pipe centerline forming a "core-peak" void fraction distribution instead of a "wall-peak" void profile that is commonly observed in smaller diameter pipes (Cheng et al., 1998; Yoneda et al., 2002; Shen et al., 2005). Herringe and Davis (1976), however, indicated that the void fraction profile was also dependant on the size of the bubbles, and obtained a core-peak void profile in a 50.8 mm diameter pipe by introducing larger bubbles to the flow. This was later corroborated by Nakoryakov et al. (1996) in a 14.8 mm pipe, where the void profile changed from a wall to a core peak when the gas injector was changed to obtain larger bubble diameters (D_b) for the same liquid and gas superficial velocities (J_f and J_g

* Corresponding author. Tel.: +1 905 545 9140x24998; fax: +1 905 572 7944.
E-mail address: chingcy@mcmaster.ca (C.Y. Ching).

0301-9322/$ - see front matter
doi:10.1016/j.ijmultiphaseflow.2008.01.007

respectively). On the other hand, a wall-peak void distribution was observed at relatively low area averaged void fraction flows ($\langle\alpha\rangle \lesssim 4\%$) in a 200 mm pipe when the bubble diameter was relatively small (Ohnuki and Akimoto, 2000; Shoukri et al., 2003; Shen et al., 2005; Shawkat et al., 2007).

Prasser et al. (2005) observed larger diameter bubbles in a 194 mm diameter pipe compared to that in a 52.3 mm diameter pipe at the same superficial velocities. Their measurements showed that the bubbles moved more freely and with more deformation in the larger diameter pipe. This is consistent with the experiments of Zun (1988) and Kariyasaki (1987), which indicated that larger bubbles tend to migrate toward the pipe centerline and form core-peak void distributions. Esmaeeli et al. (1994) and Ervin and Tryggvason (1997) attributed the change in the void fraction profile mainly to the deformation of the bubbles by analyzing the bubble trajectories for both spherical and deformed bubbles. They found that deformed bubbles tend to move toward the center of the pipe and suggested that the lift force (F_L) can reverse its direction as the bubbles are deformed. Based on experiments on a train of bubbles in an uniform shear flow, an analytical model for the lift coefficient (C_L) was introduced by Tomiyama et al. (2002). The model indicated that the lift force reversed its direction towards the pipe centerline for a relatively large bubble diameter of about 5.8 mm in air–water flow. They suggested that the reversal in the direction of the lift force was the main reason for the core-peak void profiles in large diameter pipes. Shoukri et al. (2003) and Shawkat et al. (2007), however, obtained a core-peak void distribution at smaller D_b in the range of about 3-5 mm, which corresponds to a positive C_L according to the model of Tomiyama et al. (2002).

The formation of core-peak void profiles was also related to the effect of the liquid turbulence structure around the bubbles (Ohnuki and Akimoto, 2000). This effect was first introduced by Lahey et al. (1993) in the form of an interfacial force called the "turbulent dispersion force" (F_{td}), which accounts for the diffusion effect of the surrounding liquid turbulence on the bubble motion. Ohnuki and Akimoto (2000) suggested that in upward bubbly flow this force could overcome the lift force and move the bubbles towards the centerline. Ohnuki and Akimoto (2001) compared the void fraction and turbulent velocity profiles in small and large diameter pipes for the same bubble diameter, to approximately equalize the effect of the lift force, and suggested that the turbulence dispersion force is related to the ratio between the bubble diameter to the liquid turbulence integral length scale. However, the lack of data for the liquid turbulence structure in large diameter pipes prevented a clear physical explanation of the turbulence effect on the direction of bubble migration.

Most previous investigations of the liquid turbulence in bubbly flow have been performed in pipes with diameter ranging from about 15 mm to 60 mm (Serizawa et al., 1975; Sato and Sekoguchi, 1975; Theofanous and Sullivan, 1982; Michiyoshi and Serizawa, 1986; Wang et al., 1987; Liu and Bankoff, 1993a,b; Hibiki and Ishii, 1999). In general, the average liquid velocity (U) profiles were found to be more uniform in the core region compared to the single-phase case. Theofanous and Sullivan (1982) and Wang et al. (1987) noticed a slight increase in the average liquid velocity near the radial location of the maximum void fraction, and this phenomenon was called the "Chimney Effect". It was conjectured that the increase in velocity was due to the extra driving force due to the additional bubbles in this region. The radial distribution of the axial and the radial turbulence intensities (u/U and v/U) was similar to that in single-phase flow, but more uniform in the core region indicating less turbulent diffusion in this region. The Reynolds shear stress $(\overline{-u'v'})$ showed a gradual increase towards the wall in the core region with a sharp increase in the near-wall region. The values were found to be much higher than the corresponding single-phase flows, especially near the wall ($r/R \gtrsim 0.97$). Compared to single-phase flow at the same J_f, a turbulence suppression was observed in the central region when the J_f exceeded approximately 1 m/s for area average void fraction ($\langle\alpha\rangle$) less than about 5% (Michiyoshi and Serizawa, 1986; Liu and Bankoff, 1993a; Hibiki and Ishii, 1999).

There have been far fewer studies of the liquid turbulence structure in large diameter vertical pipes. Ohnuki and Akimoto (2000) investigated the liquid average and fluctuating velocity distributions at high liquid superficial velocity of about 1 m/s in a 200 mm diameter pipe. For the same J_f and J_g, no significant difference in the magnitude and the shape of the liquid average velocity profile was noticed in the core region compared to that in small diameter pipes. However, near the pipe wall the average velocity was lower in the larger diameter pipe. The axial fluctuating velocity profile was similar to that in smaller diameter pipes. Shawkat et al. (2007), in a 200 mm diameter pipe, showed that the average liquid velocity profiles were more uniform than the single phase profile for a wall-peak void fraction profile, while having higher average velocities in the core region for core peak void fraction profiles. Their results indicated, generally, an increase in the turbulence intensity when the bubbles are introduced into the flow. However, a turbulence suppression was observed close to the wall at a very low void fraction and a high J_f.

Near the pipe wall the effect of the wall lubrication force tends to move the bubbles away from the wall (Antal et al., 1991). The effect of this force is generally limited to about two bubble diameters from the pipe wall (Lopez de Bertodano et al., 1994; Troshko and Hassan, 2001). Outside this range, it could be argued that the balance between the lift and turbulent dispersion forces govern the radial migration of the bubbles and hence determines the void fraction profile. The pipe diameter is expected to affect the flow characteristics that in turn determine the value and the direction of these forces. To investigate this balance, however, more information is required regarding the liquid turbulence structure, especially in large diameter pipes. Thus, the objective of this study is to investigate the local distribution of the bubble and liquid turbulence characteristics for two-phase bubbly flow in a 200 mm diameter vertical pipe. In particular, the main flow parameters that characterize the effect of the pipe diameter on the radial motion of the bubbles and hence the shape of the void fraction profile are investigated.

2. Experimental test facility and data reduction

A schematic of the experimental test facility is shown in Fig. 1. Filtered water and air are used as the liquid and gas phases. The two-phase flow is established in the larger diameter pipe (riser) and returns in the smaller pipe (downcomer). The riser is made of 200 mm diameter transparent acrylic tubing and is 9.56 m in length. The riser extends 0.5 m into a phase-separation tank and discharges the two-phase mixture at a level higher than the liquid level in the tank to avoid reverse flow. An angled reflector and a baffle plate were welded to the tank to enhance the phase separation. The liquid phase is then returned in the downcomer, which is made of 100 mm diameter PVC pipe, with its upper portion (1.5 m length) made of acrylic to observe the flow and ensure no air is returned. Air was introduced to the flow through a shower head injector with 550 holes of 1 mm diameter at the bottom of the riser. A honeycomb flow straightener and a coarse grid mesh were installed downstream of the injector to reduce bubble swirl and improve bubble distribution. The air and water flow rates were measured using sharp edge orifices installed in the downcomer and the inlet air line. Two pneumatic valves on the water and air lines were used to control the flow rates remotely. A cooling system consisting of two heat exchangers placed in the separation tank after the buffer plate and a dedicated chiller was used to maintain the water temperature at 24.5 ± 0.1 °C during the operation of the loop.

The bubble characteristics were measured using a dual optical probe. The vertical and horizontal distances between the probe tips were 1.16 mm and 1 mm. The liquid turbulence characteristics were measured using hot film anemometry. A single TSI 1210–60W hot film with overheat ratio 1.08 was used to measure the axial average and turbulent velocities for all flow conditions, while the radial turbulent velocity and Reynolds stress were measured for a selected number of flow conditions using a Dantec 55R63

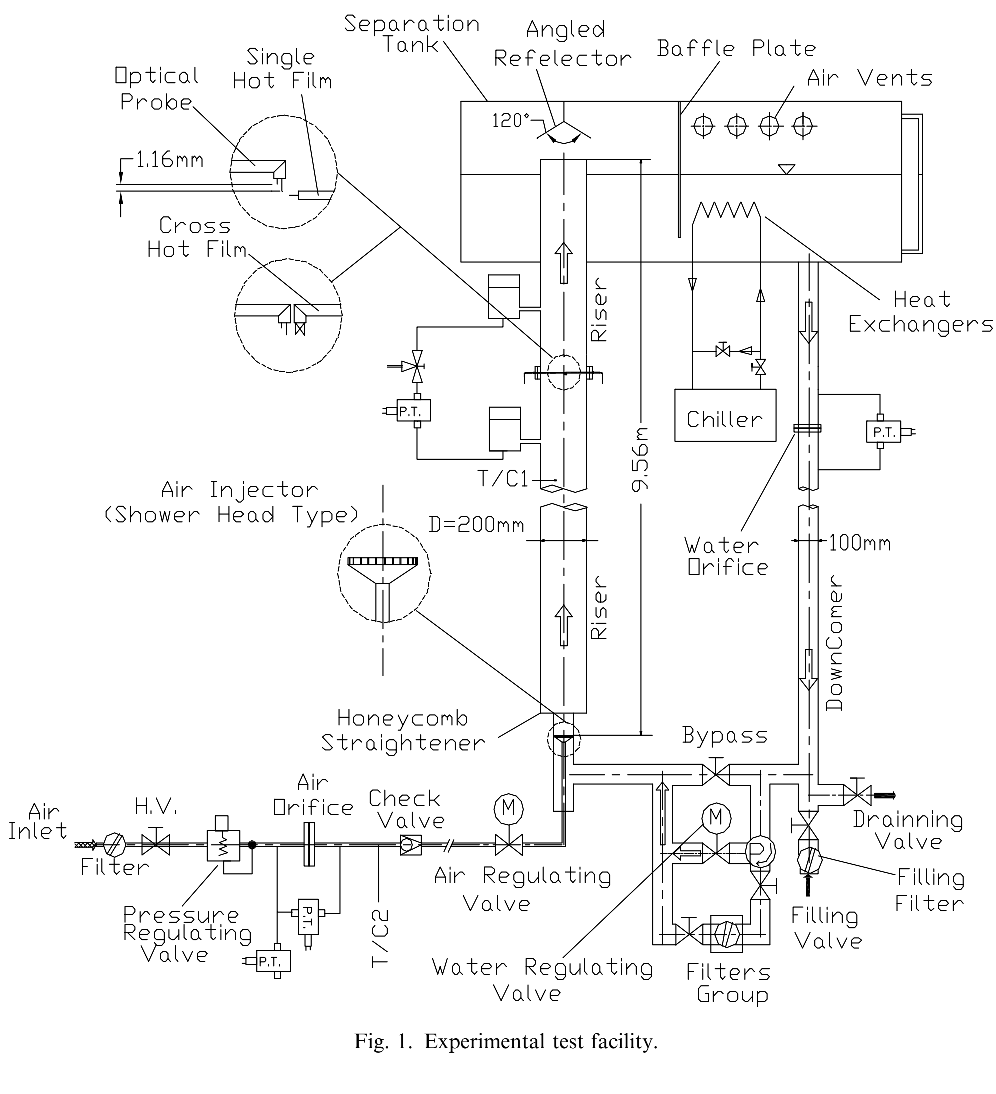

Fig. 1. Experimental test facility.

X-hot film with overheat ratio 1.06. The optical and hot-film probes were mounted on separate traverse mechanisms with 0.01 mm resolution. The data was acquired using a 16bit A/D converter interfaced to a PC using LabView software. For both optical and hot film probes, the data were acquired at a sampling frequency of 10 kHz for 80 s, which was found sufficient to obtain statistically steady values. However, at low J_g conditions a sampling time of 120 s was used due to the smaller bubble population in this case.

The hot films were calibrated in the flow loop by operating it with only water and using the centerline single-phase velocity, assuming a $(1/n)$ power law distribution for the velocity profile (where $n = 2.95Re^{0.0805}$) (Schlichting, 1979). For the cross hot-film the effective angle concept described by Browne et al. (1989) was used to decompose the signal into its two components. The reliability of the single and cross hot film measurements were checked by performing a number of single-phase measurements using only water and comparing the average liquid velocity and Reynolds stresses, (U, u', v' and $\overline{u'v'}$), with the experimental data of Laufer (1954) and Lawn (1971). The average velocity and Reynolds stresses were in good agreement with the experimental data, with a maximum deviation near the wall ($r/R > 0.85$) of approximately ±6% for the average velocity, ±10% for the turbulent intensities, and ±11% for the Reynolds shear stress.

A combined amplitude and slope threshold method was used to separate the phases in both the optical probe and hot-film signals as described by Wang and Ching (2001) and Farrar et al. (1995). A linear interpolation was used to replace the gaps that arose from removal of the gas phase signal to obtain a continuous liquid phase signal, as described by Shawkat et al. (2007). For the cross hot-film, to ensure the correct correlation between the two output signals, the voltage drops due to the gas phase were removed from both signals simultaneously, even if only one of the signals showed a voltage drop. The bubble and the liquid turbulence characteristics were calculated as described by Liu and Bankoff (1993a,b). The void fraction and the bubble frequency (defined as the number of bubbles passing the measurement location per unit time) presented in this study were obtained from the front optical probe, and these results were within ±3% of those determined from the rear probe. The average bubble diameter was estimated as the most probable value of the chord lengths (x_b) that represents the bubble diameter. This value was obtained by filtering the optical probe signals twice; first using the method of Revankar and Ishii (1992) to ensure that only bubbles that hit both probe tips in sequence were used, and second to exclude bubbles that hit the probe away from the bubble centerline. Here, the bubble were assumed spherical and moving vertically upward. The bubble diameter was also calculated using the normalized chord length probability density function ($\mathrm{PDF}(x_b)$) of the unfiltered signals, as suggested by Uga (1972) and Liu (2002)

Table 1
Relative uncertainty of the main measured quantities

Quantity	Uncertainty
U, and u (single-phase, for single hot-film)	±2.6%
U, and u (single-phase, for cross hot-film)	±3–5%
U, and u (two-phase, for single hot-film)	±3.7%
U, and u (two-phase, for cross hot-film)	±6–9%
v (single phase)	±3–5%
v (two-phase)	±6–9%
$-\overline{u'v'}$ (single-phase)	up to 0.88 cm^2/s^2 or 10%
$-\overline{u'v'}$ (two-phase)	3–8.5 cm^2/s^2 or up to 13%
α or $\langle\alpha\rangle$	14%

$$D_b = 1.5 \int_0^{\infty} x_b \cdot \mathrm{PDF}(x_b)\, dx_b \quad (1)$$

The results from the two methods agreed to within ±4.5%.

The data were taken 42 diameters (8400 mm) downstream from the location where the air was introduced. The liquid and gas superficial velocities (J_f and J_g) were in the range 0.2–0.68 m/s and 0.0–0.18 m/s, respectively. The corresponding area average void fraction varied from 0% to 15.4%, while the area average bubble diameter ($\langle D_b\rangle$) was in the range of 3-6 mm. The experimental uncertainties of the hot-film measurements were estimated according to the method of Yavuzkurt (1984). The uncertainty in the void fraction was estimated by comparing the measured area averaged void fraction with that obtained from the liquid phase integral momentum equation by measuring the axial pressure drop along the test section and using the model suggested by Beyerlein et al. (1985) to account for the wall shear stress. The details of the uncertainty analysis are given in Shawkat (2007) and are summarized in Table 1.

3. Results and discussion

3.1. Bubble characteristics

The radial void fraction distributions at the different liquid superficial velocities are shown in Fig. 2. At each liquid superficial velocity, the profiles for different J_g are presented. As expected, increasing J_g at a constant J_f increases the void fraction while an increase in J_f results in a decrease in the void fraction. For low J_f and J_g flows, the void fraction profiles are nearly uniform with a tendency to form a peak near the pipe wall as shown in Fig. 2a–c for J_g in the range 0.005–0.015 m/s, corresponding to $\langle\alpha\rangle \lesssim 4\%$. The wall peak becomes more pronounced at higher J_f, as shown in Fig. 2d–f for the same range of $\langle\alpha\rangle$. The location of the wall-peak moves closer to the pipe wall as J_f is increased. For example, in Fig. 2d–f for J_g of 0.015 m/s, the peak location changed from r/R of 0.85 to 0.925 as J_f increased from 0.45 to 0.68 m/s, which corresponds to approximately 3.5–2 $\langle D_b\rangle$ from the pipe wall. For constant J_f, an increase of J_g typically reduces the wall-peak and causes more bubbles to migrate toward the

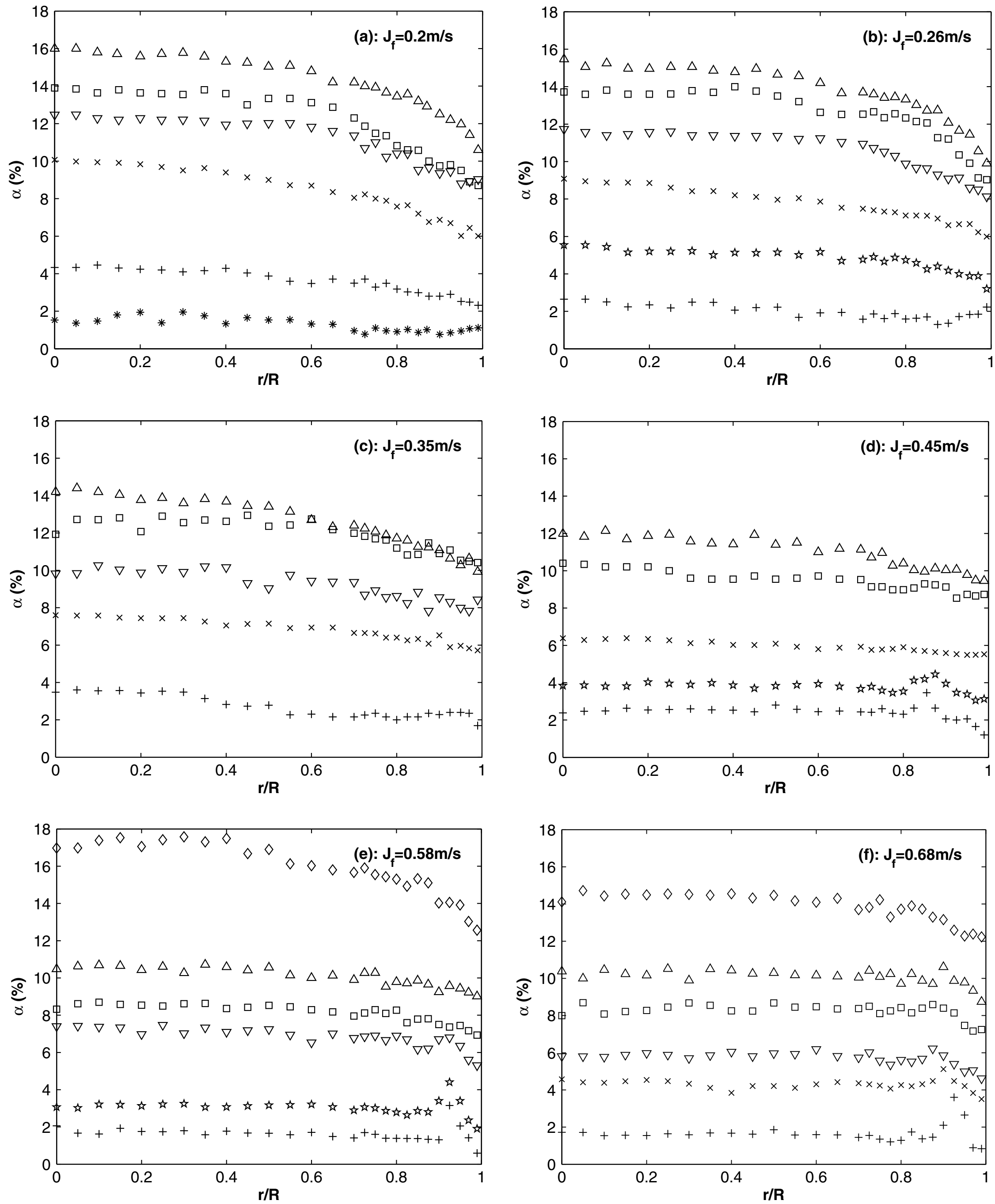

Fig. 2. Radial distribution of the void fraction at different J_f for J_g of [∗ 0.005, +0.015, ☆ 0.03, ×0.05, ▽ 0.065, □ 0.085, △ 0.1, and ◇ 0.18 m/s].

pipe centerline to form core-peak profiles. For high J_g, corresponding to $\langle\alpha\rangle \gtrsim 4\%$, the core-peak profiles are more pronounced at the low J_f flows, and the profiles become more uniform as the liquid flow rate is increased. This indicates that the tendency of bubbles to migrate toward the centerline decreases as J_f is increased for constant J_g. The change in the wall-peak profiles with the flow conditions is similar to that in smaller diameter pipes (Michiyoshi and Serizawa, 1986; Wang et al., 1987; Liu and Bankoff, 1993b), where a more pronounced wall peak was observed at high J_f flows. In small diameter pipes, however, the wall-peak became more distinct as J_g was increased for constant J_f. In the cases where a core-peak distribution was observed in small diameter pipes, the profiles were more distinct than in the larger diameter pipe, with a higher difference between the void fraction at the centerline and near the wall. For both types of void distributions, at the same J_f and J_g, the area averaged void fraction in the larger diameter pipe was smaller than the corresponding values in small diameter pipes.

The corresponding bubble frequency profiles are shown in Fig. 3. In general, the profiles have the same trend as the

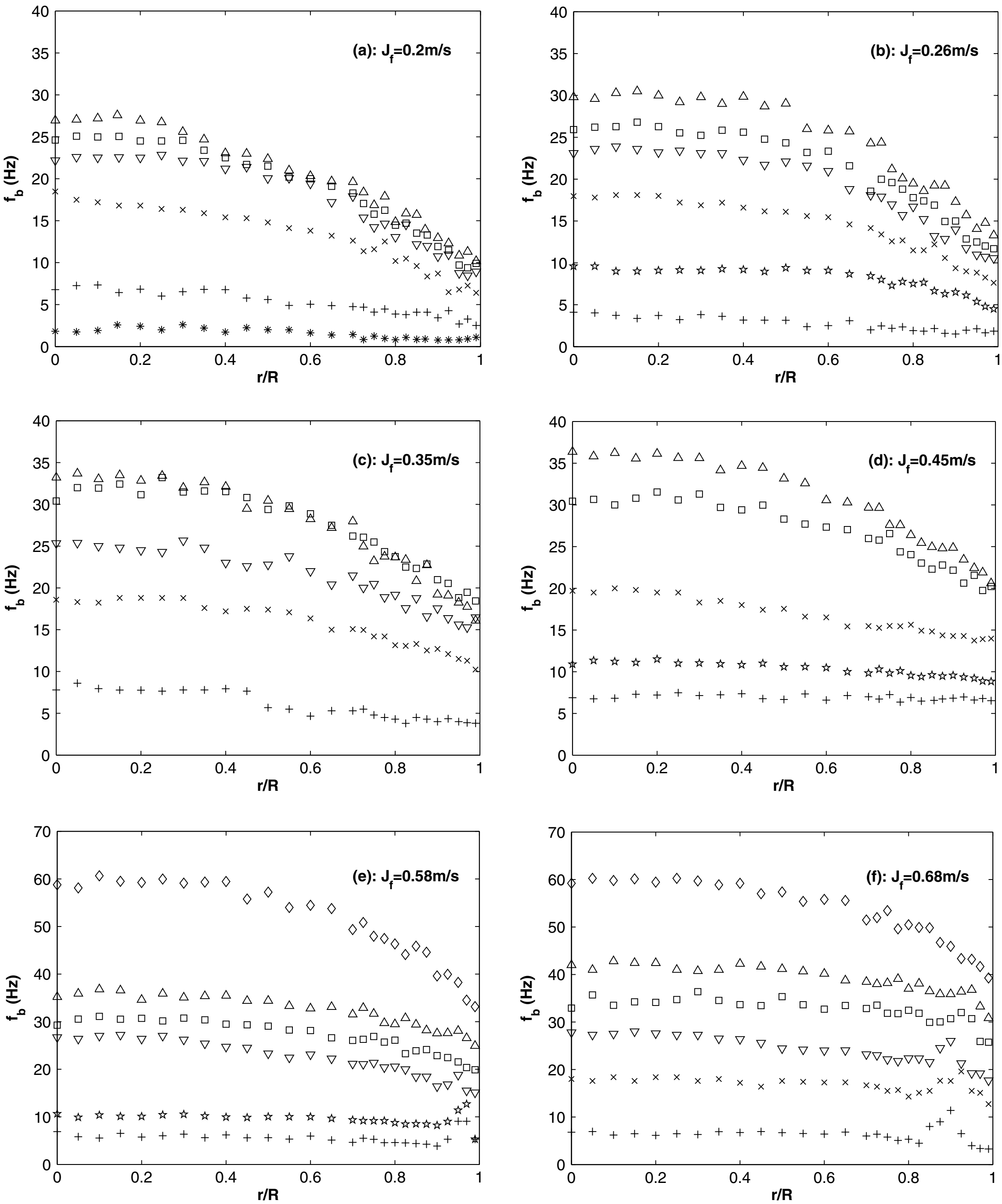

Fig. 3. Radial distribution of the bubble frequency at different J_f for J_g of [$*$ 0.005, $+$0.015, ☆ 0.03, $\times$0.05, ▽ 0.065, □ 0.085, △ 0.1, and ◇ 0.18 m/s].

void fraction profiles, where the location of the maximum frequency approximately coincides with the location of the maximum void fraction. However, relatively small void wall-peaks did not show the same significant influence on the bubble frequency as shown in Fig. 3d, where no distinct wall-peak is observed for $J_g \leqslant 0.03$ m/s. Increasing either J_g or J_f increases the bubble frequency. The increase in bubble frequency due to an increase in J_f can be attributed to an increase in the bubble break-up in the developing region. This is also consistent with the decrease in the bubble diameter as J_f is increased for constant J_g as will be discussed later. In small diameter pipes, the bubble frequency profiles had the same trend as the void fraction profiles. However, the measurements of Liu and Bankoff (1993b) in a 38.1 mm diameter pipe showed that an increase in J_f decreased f_b in the core region and increased it in the wall region ($r/R \gtrsim 0.8$). The present wall-peak profiles do not exhibit these characteristics. The bubble frequency is dependant on both the void fraction and bubble diameter. In large diameter pipes, the mechanisms that govern the

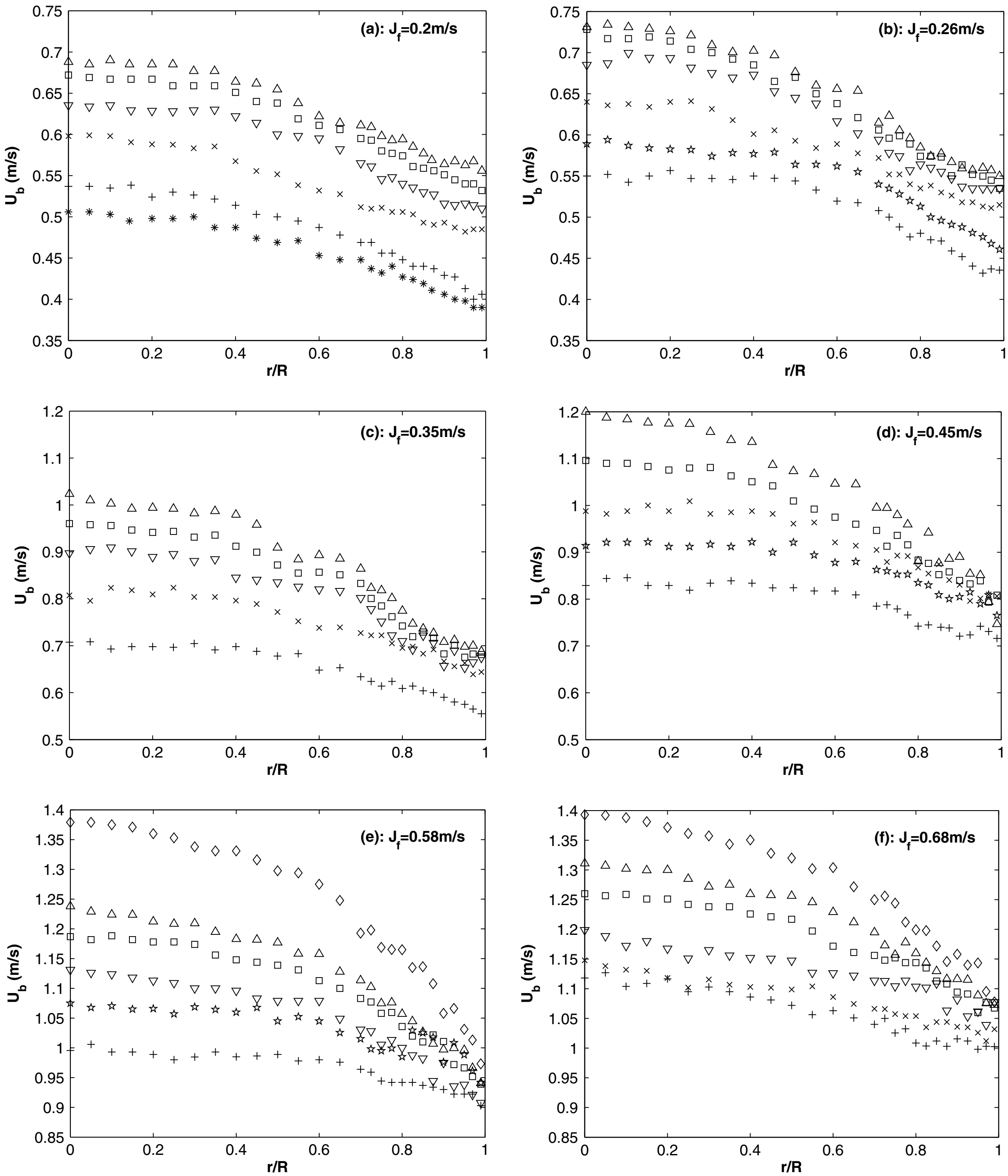

Fig. 4. Radial distribution of the bubble velocity at different J_f for J_g of [$\ast$ 0.005, +0.015, ☆ 0.03, × 0.05, ▽ 0.065, □ 0.085, △ 0.1, and ◇ 0.18 m/s].

bubble break-up and coalescence are likely to be different due to the change in the liquid turbulence structure around the bubbles as the flow domain changes.

The bubble velocity distributions are shown in Fig. 4. An increase in J_f or J_g increases the bubble velocity. In general, the bubble velocity distribution is parabolic, with the bubbles having a higher velocity at the centerline for both wall and core-peak void profiles. Increasing J_g causes a higher increase in U_b at the centerline compared to that near the wall. On the other hand, changing J_f for the same J_g did not cause a significant change in the shape of the profiles. Due to the buoyancy, the bubble velocity is always higher than the liquid velocity at the corresponding radial location. The increase in J_g results in larger bubbles which will move faster relative to the liquid due to the higher buoyancy force.

The radial distributions of the average bubble diameter are presented in Fig. 5. Increasing J_g for constant J_f results in larger bubble sizes, while an increase in J_f decreases the bubble size. This may be due to the suppression of bubble coalescence indicated from the increase in the bubble frequency. However, an increase in the bubble diameter was

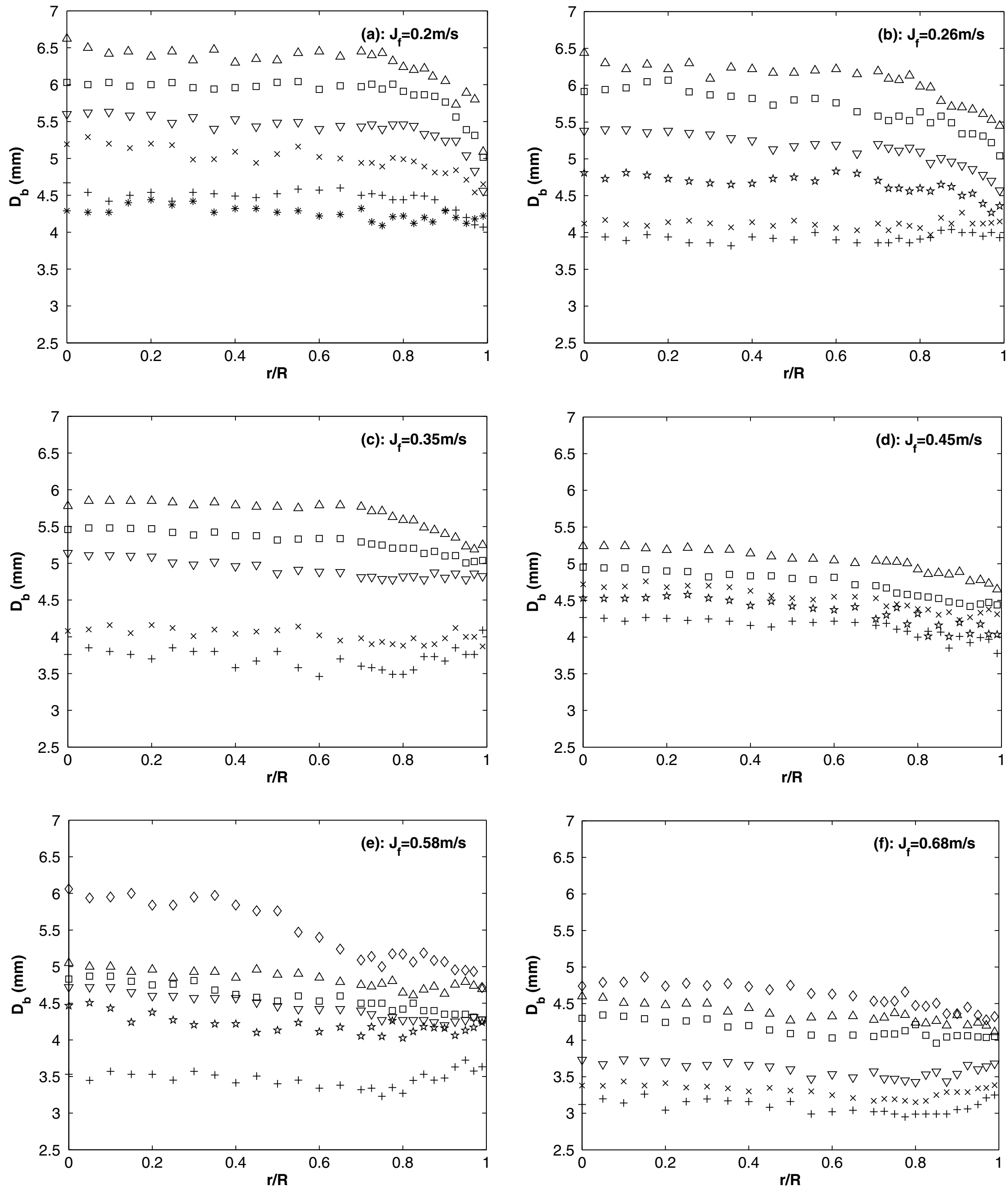

Fig. 5. Radial distribution of the bubble diameter at different J_f for J_g of [$*$ 0.005, +0.015, ☆ 0.03, × 0.05, ▽ 0.065, □ 0.085, △ 0.1, and ◇ 0.18 m/s].

observed at $J_g \lesssim 0.05$ m/s as J_f was increased from 0.35 to 0.45 m/s. This corresponds to approximately where the uniform void profile transitions to a more distinct wall-peak profile. Such a transition may result in more bubble coalescence, especially near the pipe wall. For the cases with a core-peak void fraction, the bubble diameter distributions are mainly uniform in the core region (up to $r/R \approx 0.8$), and then decrease as the wall is approached. For the wall-peak cases, the bubble diameter profiles are also uniform in the core region but show a continuous increase toward the pipe wall in the near-wall region, indicating more bubble coalescence in this region. This is different to that observed in small diameter pipes, where the bubble diameter profiles show a peak near the wall (Michiyoshi and Serizawa, 1986; Liu and Bankoff, 1993b; Hibiki and Ishii, 1999). As in the bubble frequency profiles, small void peaks did not have a significant effect on the bubble size distribution near the wall, as shown in Fig. 5d. For example, at $J_g \leqslant 0.03$ m/s the bubble diameter profiles do not show an increase in the wall region although the void profiles showed a peak in this region for this flow range (Fig. 2d).

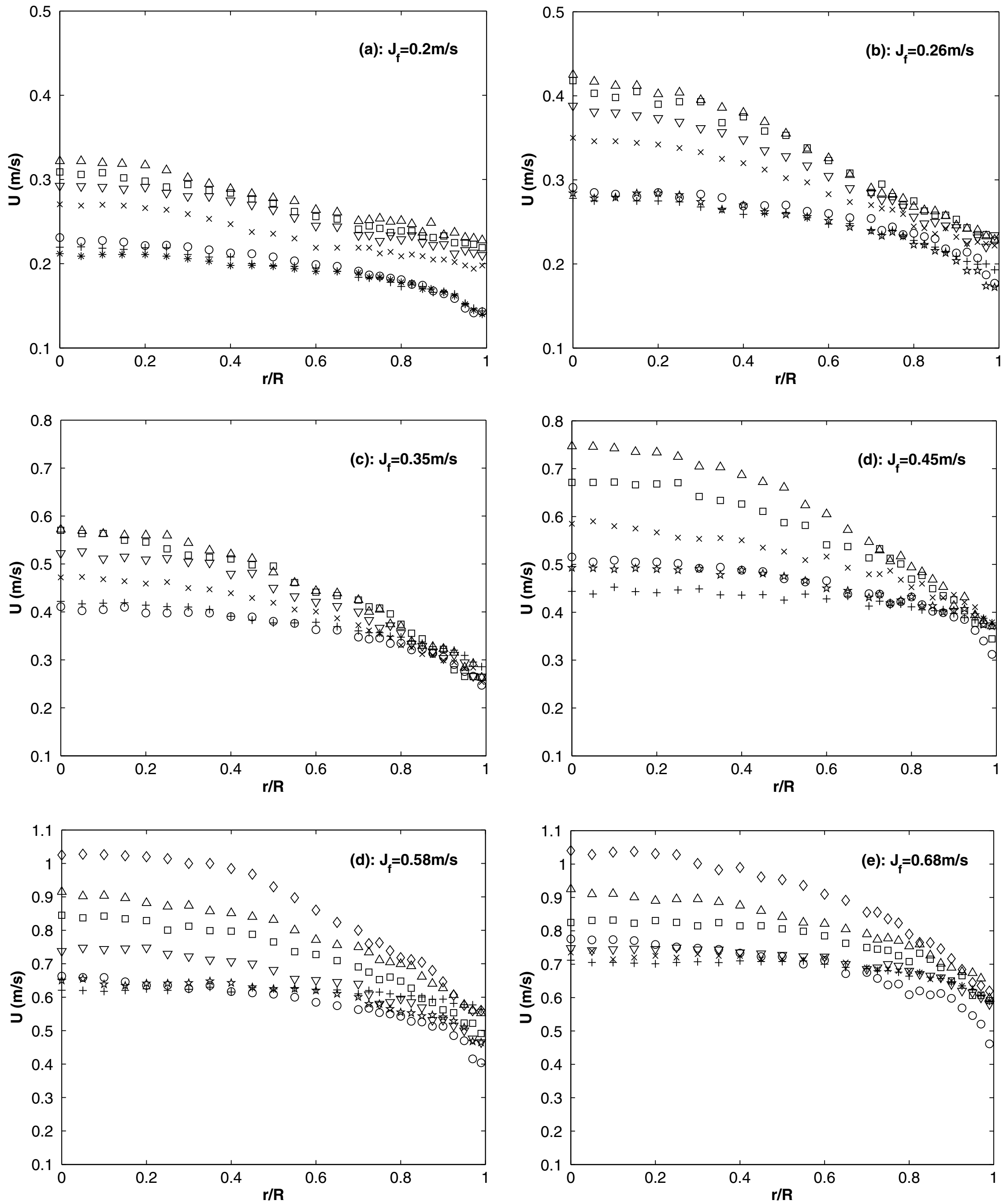

Fig. 6. Radial distribution of the liquid average velocity at different J_f for J_g of [○ 0.0, ∗ 0.005, +0.015, ☆ 0.03, × 0.05, ▽ 0.065, □ 0.085, △ 0.1, and ◇ 0.18 m/s].

3.2. Liquid velocity and turbulence characteristics

The radial distributions of the average liquid velocity and the corresponding profiles normalized by the centerline velocity for the different flow conditions are shown in Figs. 6 and 7, respectively. The single-phase average liquid velocity profiles at the same J_f are also shown for comparison. For low J_f and J_g, the average liquid velocity profiles are similar to that of single-phase flow, but with relatively higher velocities near the pipe wall as shown in Fig. 6a–c and Fig. 7a–c for J_g of 0.005–0.015 m/s. In this flow range, the void fraction profiles are mainly uniform in the core region with a peak near the wall, which likely causes the average liquid velocity in that region to increase due to the buoyancy effect of the bubbles. For higher J_f of 0.45–0.68 m/s and low J_g, the wall-peak void profiles are more prominent resulting in higher average velocities near the wall, and a more uniform velocity in the core region as shown in Figs. 6d–f and 7d–f. For the low void fraction flow conditions, the U values in the central region are lower than the corresponding single-phase values as shown in Fig. 6, especially at the high J_f flows. This could be

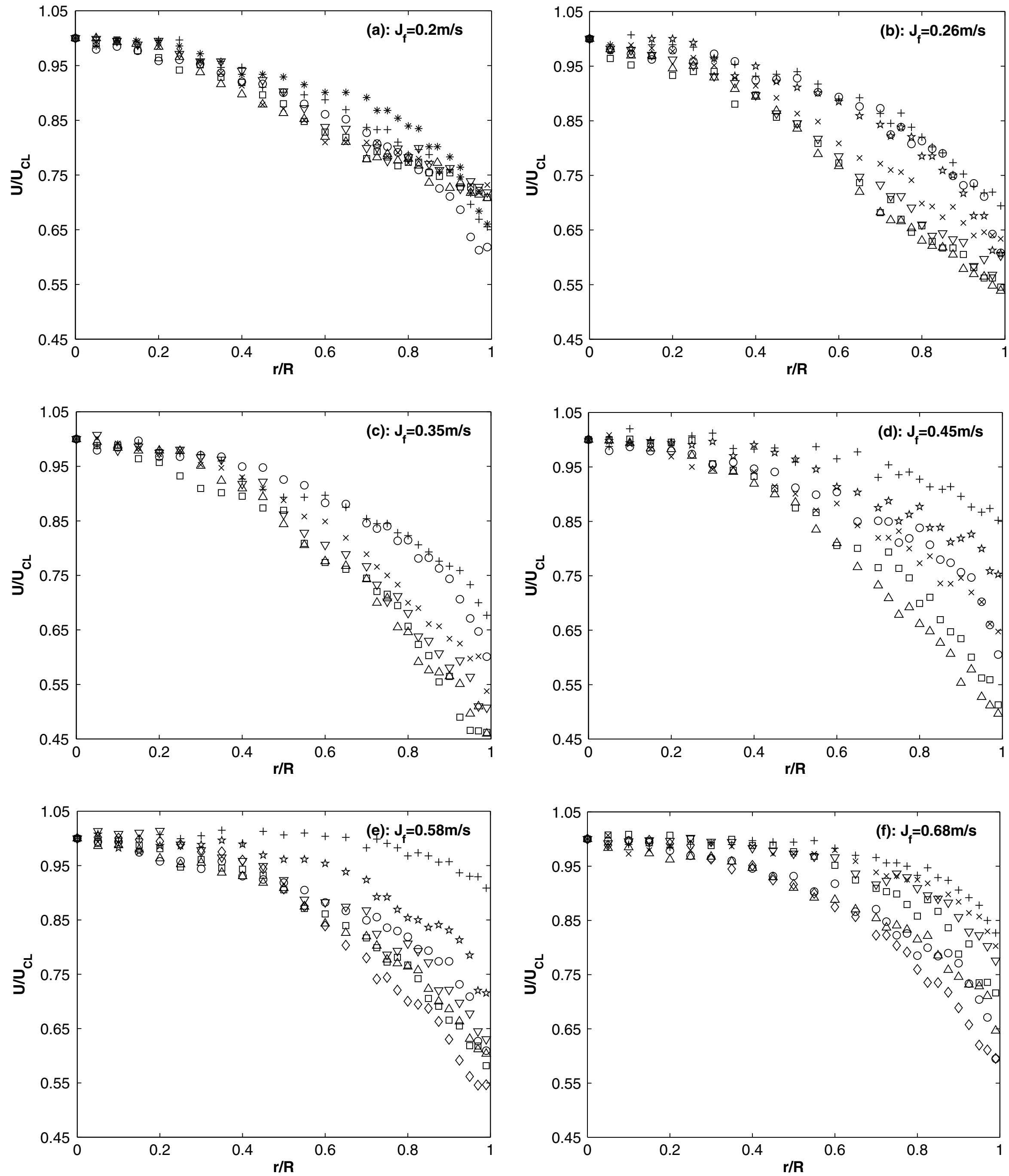

Fig. 7. Radial distribution of the normalized liquid average velocity at different J_f for J_g of [○ 0.0, ∗ 0.005, +0.015, ☆ 0.03, × 0.05, ▽ 0.065, □ 0.085, △ 0.1, and ◇ 0.18 m/s].

explained from the liquid phase mass conservation, where the increase in the average velocity near the wall has to be compensated by a decrease in its value in the central region for the same liquid flow rate. For high J_g, the void profiles change to a core-peak distribution which causes the liquid average velocity to be higher in the core region than near the wall. Consequently, the normalized velocity profiles displays a parabolic shape, with higher centerline velocities than the corresponding single-phase flow for high void fraction flows, as shown in Fig. 7 at the highest J_g. A similar effect of void fraction on (U/U_{CL}) profiles was observed by Nakoryakov et al. (1996), as the void profiles changed from a wall to a core peak distribution. Fig. 8 illustrates the radial distribution of the relative velocity between the bubbles and the average liquid velocity ($U_r = U_b - U$). At low J_f, the relative velocity tends to decrease toward the pipe wall (Fig. 8a and b). As J_f is increased, the profiles become more uniform and then increase toward the pipe wall, indicating higher turbulence in that region (Fig. 8e and f). The transition between the two trends occurs in the range of J_f between 0.35 and 0.45 m/s.

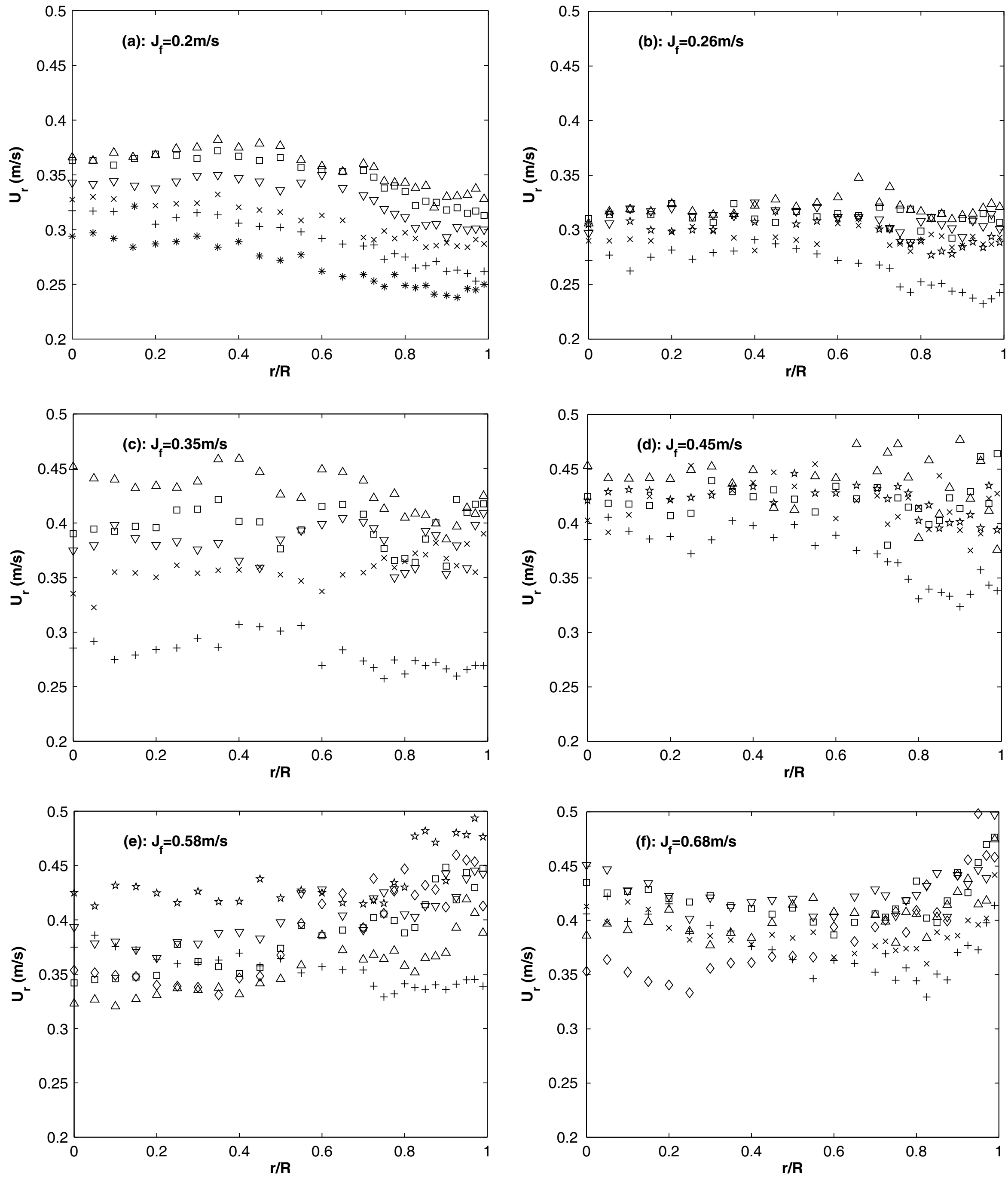

Fig. 8. Radial distribution of the relative velocity at different J_f for J_g of [∗ 0.005, +0.015, ☆ 0.03, × 0.05, ▽ 0.065, □ 0.085, △ 0.1, and ◇ 0.18 m/s].

The radial distribution of the liquid axial turbulence intensity is shown in Fig. 9. The single-phase turbulence data corresponding to the same J_f are shown for comparison. For a constant J_f, increasing J_g, generally, increases u/U for all the flow conditions. The current data shows a dramatic decrease in u/U as J_f is increased. At J_f of 0.58 and 0.68 m/s and J_g of 0.015 m/s ($\langle\alpha\rangle \lesssim 1.6\%$), a turbulence suppression relative to the single-phase flow is observed near the wall as shown in Fig. 9e and f. For the lower J_f of 0.2 and 0.26 m/s, the introduction of the bubbles increases the axial turbulent velocity in the core region more than in the near wall region, resulting in profiles that decrease toward the wall as shown in Fig. 9a and b. At the higher J_f of 0.35 and 0.45 m/s, the axial turbulent velocity near the wall increases more rapidly compared to the core region as J_g is increased, and the profiles of u/U show an increase toward the pipe wall (Fig. 9c and d). For the high J_f flows of 0.58 and 0.68 m/s, an increase in J_g causes a significant increase in u/U near the wall which results in profiles that tend to increase toward the pipe wall (Fig. 9e and f). The change in the trends of u/U profiles as J_f is increased is

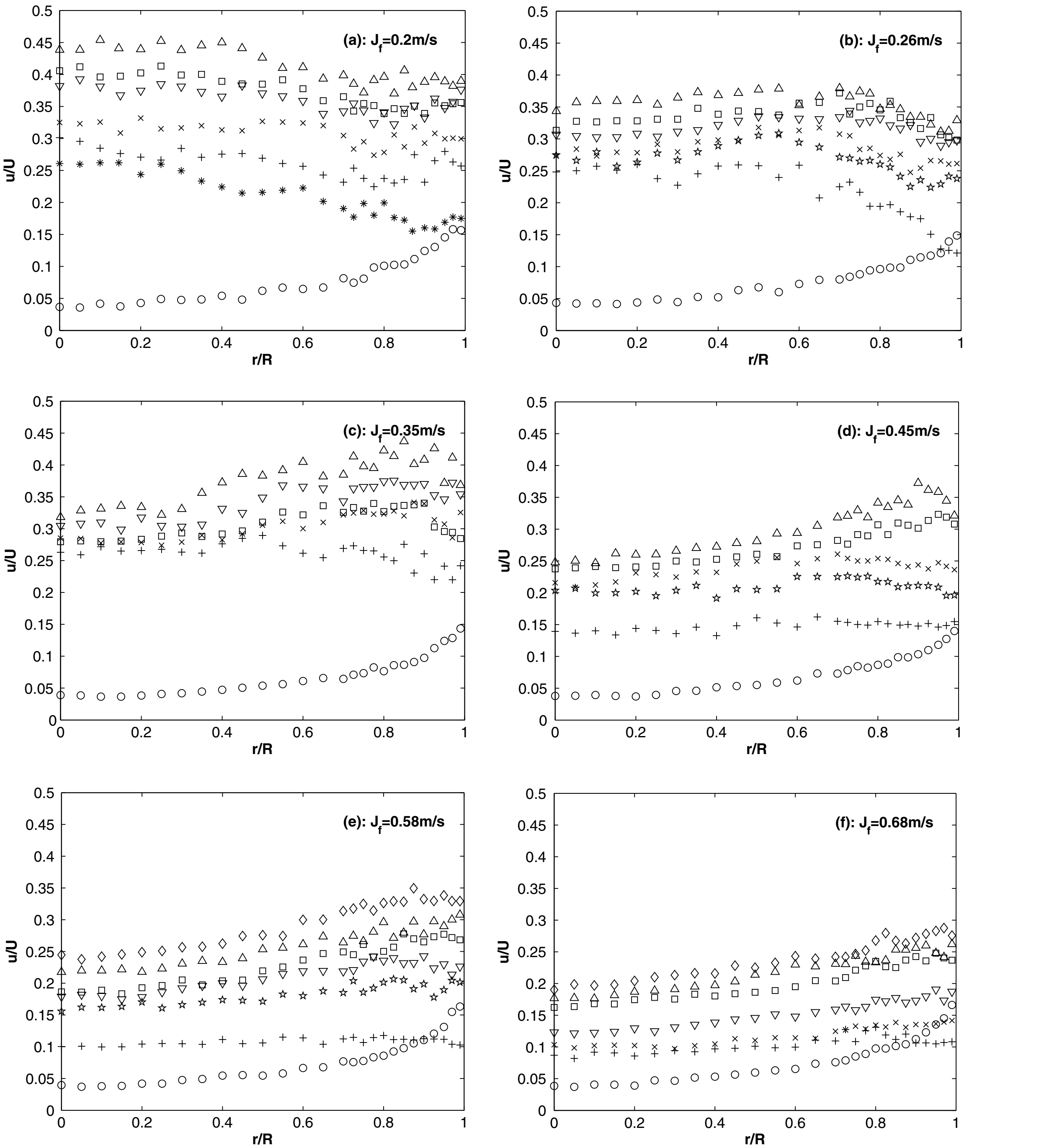

Fig. 9. Radial distribution of the axial turbulence intensity at different J_f for J_g of [○ 0.0, $*$ 0.005, + 0.015, ☆ 0.03, × 0.05, ▽ 0.065, □ 0.085, △ 0.1, and ◇ 0.18 m/s].

consistent with the change in the trends of the relative velocity profiles.

In general, the radial turbulence intensity profiles have the same trends as the axial turbulence as shown in Fig. 10. However, they become more uniform as J_f is increased without showing an increase toward the pipe wall as in the axial turbulent velocity profiles. The value of v/u was in the range 0.35–1. A turbulence suppression is observed in the v/U profiles at the same flow conditions of the u profiles. The suppression region for the radial turbulence is slightly wider than the corresponding region for the axial turbulence, especially at J_f of 0.68 m/s, where the suppression in u/U is observed at r/R of 0.9 (Fig. 9f) while for v/U it starts at r/R of 0.825 (Fig. 10f) for J_g of 0.015 m/s.

As the bubbles are introduced to the flow, the Reynolds shear stress increases significantly compared to the corresponding single phase flow as shown in Fig. 11, except for the suppression conditions. A suppression of the Reynolds shear stress is observed at J_f of 0.68 m/s and J_g of 0.015 m/s over a r/R range that starts at about 0.725, which is wider

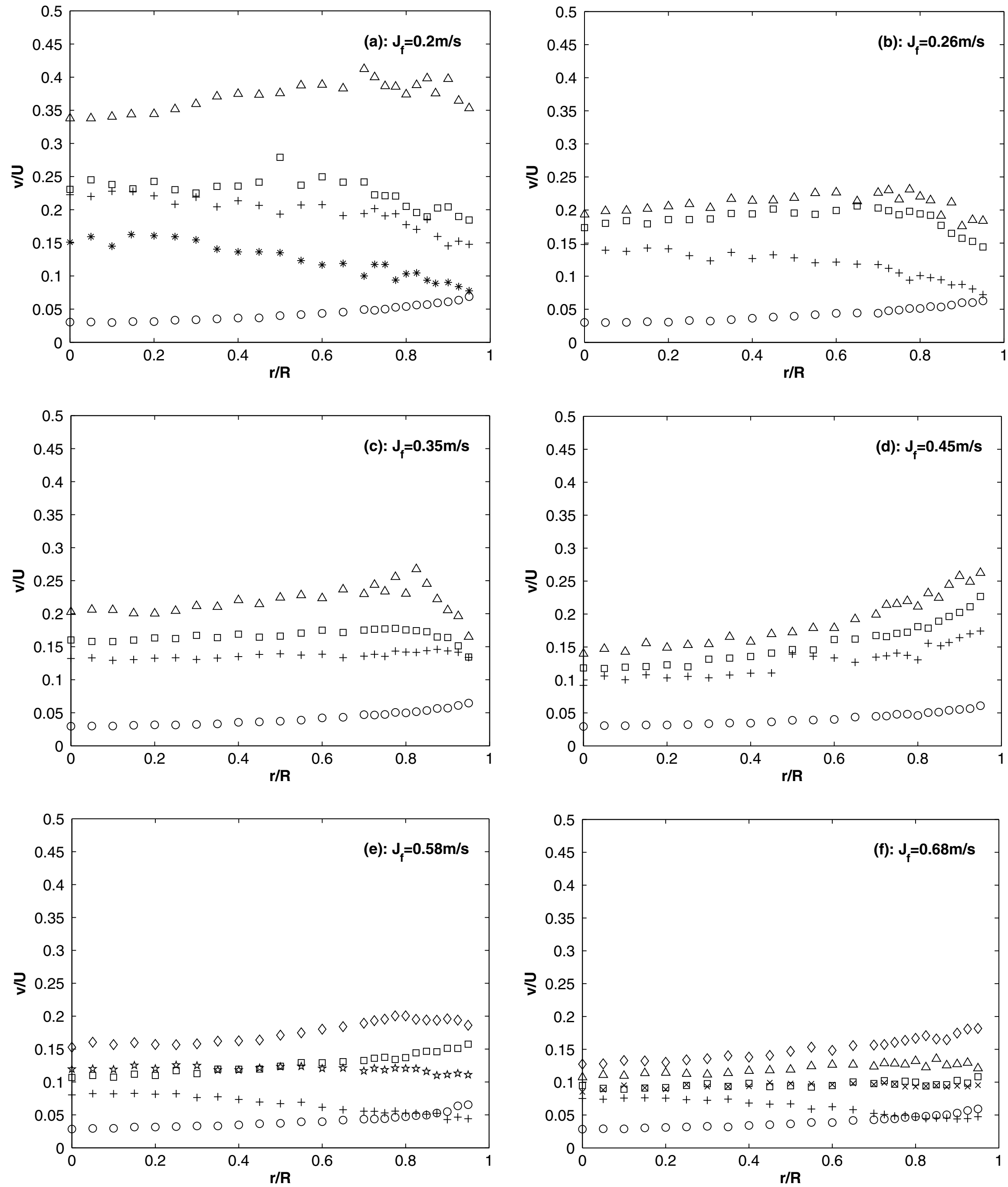

Fig. 10. Radial distribution of the radial turbulence intensity at different J_f for J_g of [○ 0.0, ∗ 0.005, +0.015, ☆ 0.03, × 0.05, □ 0.085, △ 0.1, and ◇ 0.18 m/s].

than that observed for both turbulent velocities. Increasing J_f decreases the shear stress where a smaller bubble diameter and void fraction are found. For the wall-peak void flows, the Reynolds shear stress generally increase toward the pipe wall with the values being slightly higher than that in single phase flows in the near-wall region. When the void fraction profiles display a core-peak, the Reynolds shear stress profiles show a maximum around r/R of 0.5–0.8, which becomes more distinct at $J_f \geqslant 0.35$ m/s. The maximum of the shear stress, however, does not necessarily coincides with the maximum of the void fraction.

3.3. Net radial interfacial force on the bubbles

The net radial interfacial force on the bubbles can be estimated from the one dimensional steady radial momentum equations. These equations for the liquid and gas phases in cylindrical coordinates are

$$0 = -(1-\alpha)\frac{\partial \overline{P_L}}{\partial r} - \rho_L \frac{1}{r}\frac{\partial (1-\alpha) r\overline{v'^2}}{\partial r} + \rho_L (1-\alpha)\frac{\overline{w'^2}}{r} + (\overline{p_{I_L} - P_L})\frac{\partial (1-\alpha)}{\partial r} + M_{r_L} \tag{2}$$

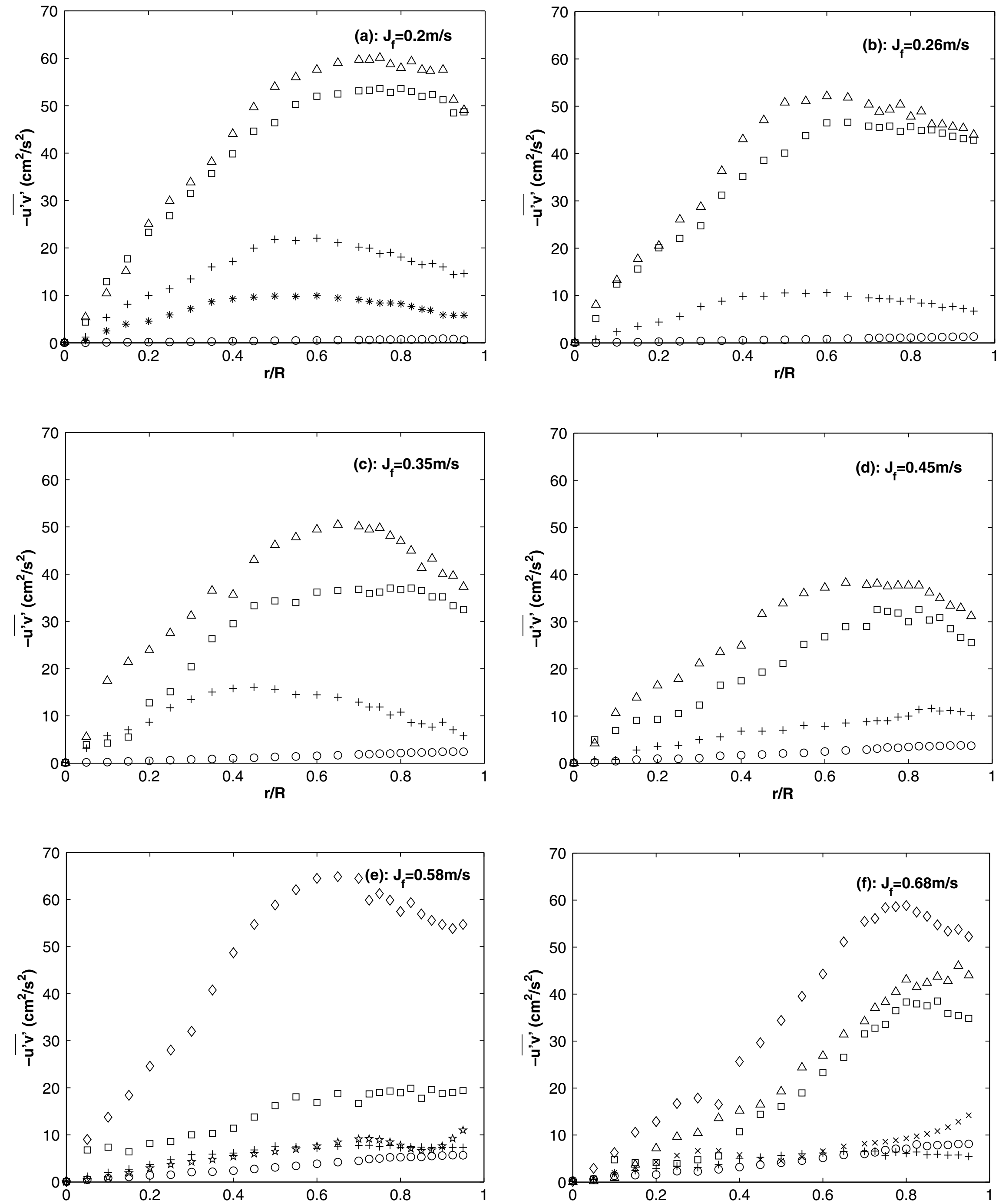

Fig. 11. Radial distribution of the Reynolds shear stress at different J_f for J_g of [○ 0.0, ∗ 0.005, + 0.015, ☆ 0.03, × 0.05, □ 0.085, △ 0.1, and ◇ 0.18 m/s].

$$0 = -\alpha\frac{\partial\overline{P_G}}{\partial r} - \rho_G\frac{1}{r}\frac{\partial(\alpha)r\overline{v_{Gas}'^2}}{\partial r} + \rho_G(\alpha)\frac{\overline{w_{Gas}'^2}}{r} + (\overline{p_{I_G} - P_G})\frac{\partial(\alpha)}{\partial r} + M_{r_G} \quad (3)$$

where P, p_I, ρ, w and M_r are the phasic pressure, interface pressure, density, azimuthal turbulent velocity and net radial interfacial force in the r-direction, respectively. The subscripts L and G indicate the liquid and the gas phases respectively, while the overbar indicates a time average. Neglecting the effect of the surface tension leads to,

$$M_{r_L} = -M_{r_G} \quad (4)$$

For a single interface pressure (p_I)

$$p_{I_L} = p_{I_G} = p_I \quad (5)$$

Assuming no pressure gradient in the gas phase results in,

$$p_{I_G} = P_G \quad (6)$$

The phasic pressure difference $(p_I - P_L)$ could be expressed using Eqs. (5) and (6) as Lahey et al. (1993),

$$\overline{p_I - P_L} = \overline{P_G - P_L} = \rho_L[C_p(U_r)^2(1-\alpha)] \quad (7)$$

where C_p is an empirical constant and its value is typically between 0.25 for single bubbles and 1.7 for a swarm of bubbles (Lopez de Bertodano et al., 2004; Troshko and Hassan, 2001). In the current study, C_p was taken equal to 1 as recommended by Lahey et al. (1993) for bubbly flow in vertical conduits.

By neglecting the gas turbulent stresses relative to the liquid stresses and adding $\alpha\frac{\partial \overline{P_L}}{\partial r}$ to both sides of Eq. (3), and using Eqs. (4)–(6), the momentum equations could be re-written as

$$0 = -(1-\alpha)\frac{\partial \overline{P_L}}{\partial r} - \rho_L \frac{1}{r}\frac{\partial (1-\alpha) r\overline{v'^2}}{\partial r} + \rho_L(1-\alpha)\frac{\overline{w'^2}}{r} + (\overline{p_I - P_L})\frac{\partial (1-\alpha)}{\partial r} - M_{r_G} \quad (8)$$

$$\alpha\frac{\partial \overline{P_L}}{\partial r} = -\alpha\frac{\partial (\overline{p_I - P_L})}{\partial r} + M_{r_G} \quad (9)$$

Eliminating the pressure gradient from Eqs. (8) and (9) gives

$$M_{r_G} = \alpha\rho_L\left[\frac{-1}{r}\frac{\partial(1-\alpha)r\overline{v'^2}}{\partial r} + (1-\alpha)\frac{\overline{w'^2}}{r} - \frac{1}{\rho_L}\frac{\partial \alpha(\overline{p_I - P_L})}{\partial r}\right] + \alpha\frac{\partial(\overline{p_I - P_L})}{\partial r} \quad (10)$$

The local variation of M_{r_G} was estimated from Eq. (10) using the measured profiles of the liquid turbulent velocities, the relative velocity and the void fraction, and assuming $\overline{w'^2} \approx \overline{v'^2}$. The uncertainty in M_{r_G} was within ±10 to ±40%. The sign of M_{r_G} indicates the direction of the net interfacial force on the bubbles in the radial direction. In the core region of the pipe, M_{r_G} is expected to be negative for core-peak void profile flows since the net interfacial forces would move the bubbles toward the pipe centerline in this case. Likewise, positive values for M_{r_G} in the pipe core region are expected in case of wall-peak void flows. The core region, in this analysis, was defined up to the location of the maximum void fraction in case of wall-peak profiles and up to $2.5D_b$ from the wall for core-peak profiles, which correspond to $r/R \approx 0.85$.

The radial distribution of M_{r_G} for the present data is shown in Fig. 12. For J_f of 0.2 and 0.26 m/s, and the lowest J_g, the net interfacial force tends to reverse its direction near the pipe wall. This is consistent with the void profiles at these flow conditions (Fig. 2a and b) where the profiles show a small wall peak. As J_f is further increased to 0.45 m/s and the void profiles have a more distinct wall-peak, the value of the force increases up to the location of the void peak and then decreases, with negative values when the effect of the wall lubrication force becomes significant. For core-peak void flows, as J_f is increased at the same J_g, the value of $|M_{r_G}|$ decreases indicating a reduction in the migration of bubbles towards the centerline. For the wall-peak void flows, M_{r_G} increased with J_f for the same J_g resulting in a greater number of bubbles near the wall.

The net radial interfacial force on the bubbles in the core region could be decomposed into the lift and turbulent dispersion forces as

$$\overrightarrow{M_{r_G}}|_{\text{core-region}} = \overrightarrow{F_L}|_{\text{on bubbles}} + \overrightarrow{F_{td}}|_{\text{on bubbles}} \quad (11)$$

The void fraction profile in the pipe core-region will be determined by the balance between the lift and turbulent dispersion forces, which could be quantified by the ratio between their area averaged values in the core region

$$F_{\text{ratio}} = \frac{\langle F_{td}\rangle_{\text{core-region}}}{\langle F_L\rangle_{\text{core-region}}} \quad (12)$$

The lift force can be expressed as

$$F_L|_{\text{on bubbles}} = -C_L\alpha\rho_L(U_b - U)\frac{\partial U}{\partial r} \quad (13)$$

The lift coefficient is estimated using the model of Tomiyama et al. (2002), where

$$C_L = \begin{cases} \min[0.288\tanh(0.121 Re_b), f(E_{od})] & \text{for} \quad E_{od} < 4 \\ f(E_{od}) \text{ for } 4 \leqslant E_{od} \leqslant 10.7 \end{cases}$$

and

$$f(E_{od}) = 0.00105E_{od}^3 - 0.0159E_{od}^2 - 0.0204E_{od} + 0.474 \quad (14)$$

Here, Re_b and E_{od} are the bubble Reynolds number and the deformed Eötvös number based on the length of the horizontal axis of the bubbles. For prolate bubbles, which is the case in most bubbly flows (Clift et al., 1978), E_{od} is related to the traditional Eötvös $\left(\text{i.e } E_0 = \frac{g(\rho_L-\rho_G)D_b^2}{\sigma}\right)$ by

$$E_{od} = E_0(1 + 0.163E_0^{0.757})^{\frac{2}{3}} \quad (15)$$

where σ is the surface tension. From Eqs. (10), (11) and (13) the ratio between the forces could be presented as

$$\frac{F_{td}}{F_L} = -1 + \frac{-1}{C_L U_r \frac{\partial U}{\partial r}}\left[\frac{-1}{r}\frac{\partial(1-\alpha)r\overline{v'^2}}{\partial r} + (1-\alpha)\frac{\overline{w'^2}}{r} - \frac{1}{\rho_L}\frac{\partial\alpha(\overline{p_I - P_L})}{\partial r}\right] + \frac{1}{\rho_L C_L U_r \frac{\partial U}{\partial r}}\frac{\partial(\overline{p_I - P_L})}{\partial r} \quad (16)$$

The following relations are introduced to determine the order of magnitude of the different terms in the above equation:

$$\overline{v'^2} \sim \overline{w'^2} \sim KE_L$$

$$U \sim \frac{U_r}{S-1}$$

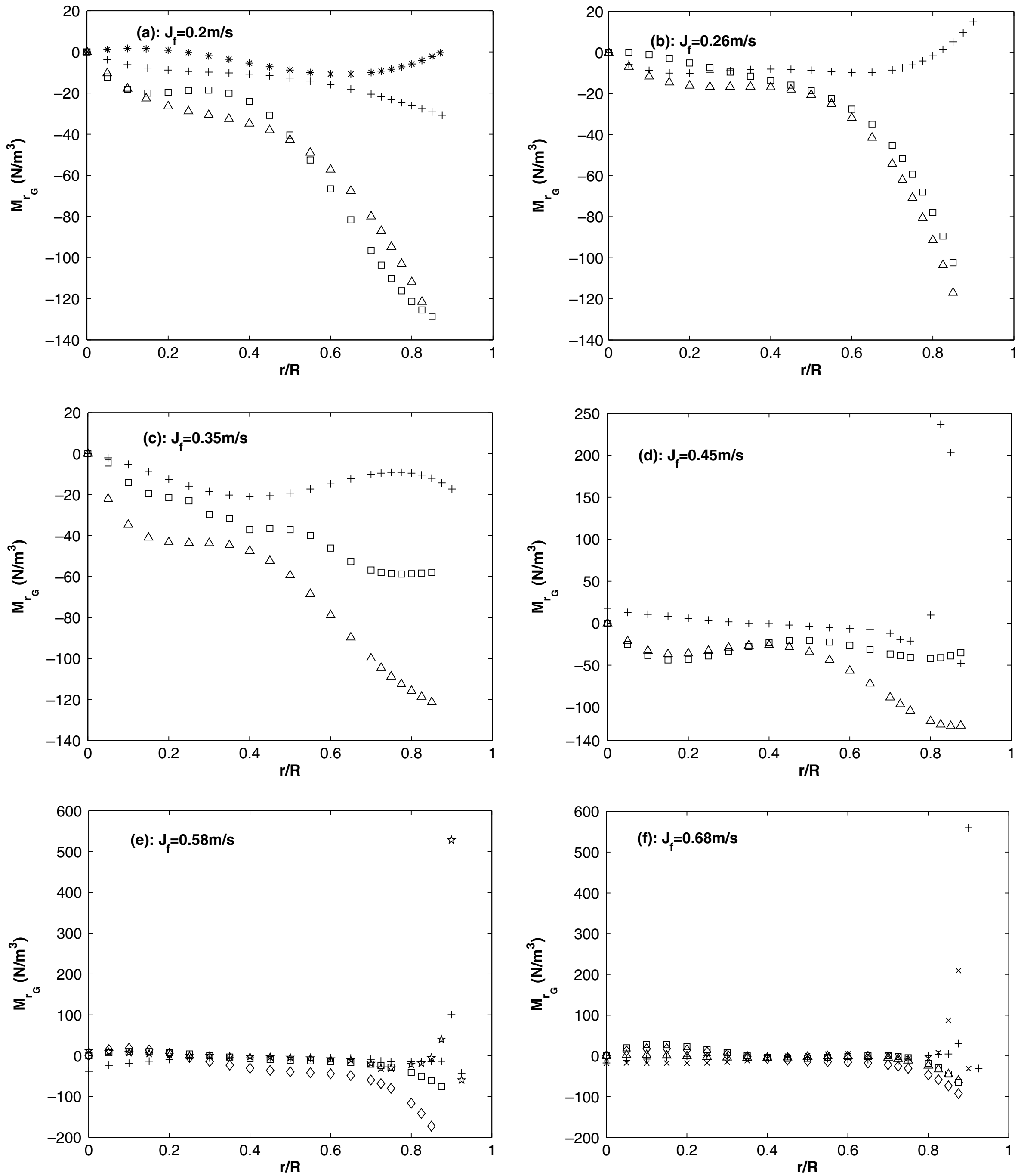

Fig. 12. Radial distribution of the net interfacial force on the gas-phase in the radial direction at different J_f for J_g [$*$ 0.005, +0.015, ☆ 0.03, × 0.05, □ 0.085, △ 0.1, and ◇ 0.18 m/s].

where S is the slip ratio. The phasic pressure difference is proportional to the relative velocity and the void fraction as shown in Eq. (7),

$$\frac{p_I - P_L}{\rho_L} \sim U_r^2(1-\alpha) \tag{17}$$

and from Tomiyama et al. (2002) the lift coefficient is proportional to Eötvös number

$$C_L \sim E_0 \tag{18}$$

Hence, the ratio $\frac{F_{td}}{F_L}$ could be represented as

$$\frac{F_{td}}{F_L} = f(\alpha, S, KE_L, U_r^2, E_0) \tag{19}$$

or using an area average over the core region as

$$F_{ratio} = \frac{\langle F_{td}\rangle_{core\text{-}region}}{\langle F_L\rangle_{core\text{-}region}} \approx f(\langle\alpha\rangle, \langle S\rangle, \langle KE_L\rangle, \langle U_r\rangle^2, \langle E_0\rangle) \tag{20}$$

The balance between the lift and turbulent dispersion forces was estimated from Eqs. (10), (11) and (13) for the current flow conditions and for the data of Michiyoshi and Serizawa (1986), Wang et al. (1987) and Liu and Bankoff (1993a,b) to represent small diameter pipes. Three cases were observed for the balance between F_L and F_{td} as D_b was increased. Fig. 13 illustrates these cases with the corresponding range of F_{ratio} for each case. In the first case, for small diameter bubbles, both forces are positive and the bubbles move toward the wall to form a wall-peak void profile. In this case F_{td} was higher than F_L. In the second case, for bubble sizes larger than case 1, F_{td} is negative and higher than F_L and the bubbles will reverse its migration direction toward the pipe centerline to form a core-peak void profile. In the final case, for larger bubbles ($D_b \gtrsim 5.8$ mm), according to the model of Tomiyama et al. (2002), the lift coefficient becomes negative and the lift force reverses it direction to form more distinct core-peak void profiles. The case of $1 \geqslant F_{ratio} \geqslant -1$, was not observed for the data sets examined here.

The flow parameters on the right hand side of Eq. (20) can be grouped into one dimensionless group, X, where

$$X = \langle S\rangle\langle E_0\rangle\langle\alpha\rangle\frac{\langle U_r\rangle^2}{\langle KE_L\rangle} \tag{21}$$

and hence

$$F_{ratio} = f(X) \tag{22}$$

The group X represents the combined effect of the slip ratio, the bubble deformation (represented by E_0), and the ratio between the apparent added turbulence kinetic energy to the liquid by the bubbles to the actual turbulent kinetic energy $\left(\frac{\langle\alpha\rangle\langle U_r\rangle^2}{\langle KE_L\rangle}\right)$. The value of X was found to be well correlated with the area averaged bubble diameter as shown in Fig. 14, which is consistent with Fig. 13. The figure shows that case 1 is associated with bubble diameters up to about of 4 mm and X less than about 3.5, while case 2 corresponds to $\langle D_b\rangle$ in the range of 4 to about 5.5 mm and X higher than 2.5. There is an overlap between the boundaries of the first and the second cases for X between 2.5 and 3.5 and $\langle D_b\rangle$ in the range of 3.8 to about 4.2, indicating a transitional zone where either a wall or core peak void profile could occur. For values of X greater than about

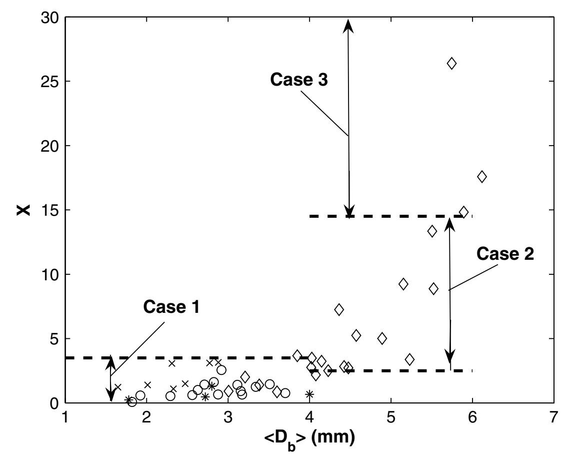

Fig. 14. The relation between the area averaged bubble diameter and the dimensionless group X for $*$ Michiyoshi and Serizawa (1986) data, × Wang et al. (1987) data, ○ Liu (1989) data, and ◇ present data.

14.5, which corresponds to D_b larger than 5.8 mm, the core-peak becomes more distinct as the lift force reverses it direction.

The value of F_{ratio} is plotted as a function of X in Fig. 15. The data fall into three distinct zones, corresponding to the three cases shown in Figs. 13 and 14. The approximate boundaries of these zones can be described as

$$\begin{cases} F_{ratio} > 1 \text{ and } X3.5 & \text{Wall-Peak (case 1)} \\ F_{ratio} < -1 \text{ and } X \in [2.5 \to 14.5] & \text{Core-Peak (case 2)} \\ F_{ratio} > 1 \text{ and } X \gtrsim 14.5 & \text{Distinct Core-Peak (case 3)} \end{cases}$$

In order to obtain a distinct bubbly flow regime, most previous experiments in small diameter pipes had $\langle D_b\rangle$ in the range 1.8–3.7 mm (Michiyoshi and Serizawa, 1986; Wang et al., 1987; Liu and Bankoff, 1993a), with corresponding

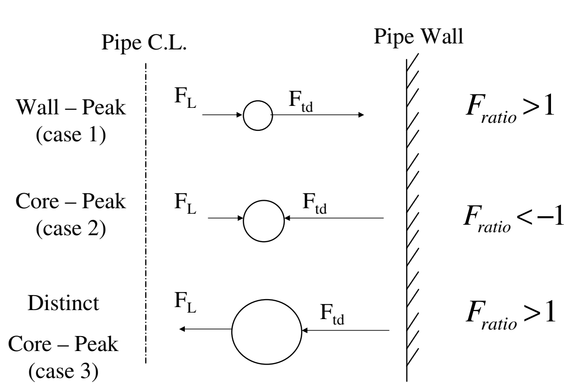

Fig. 13. The different cases for the balance between the lift and turbulent dispersion forces in the pipe core region.

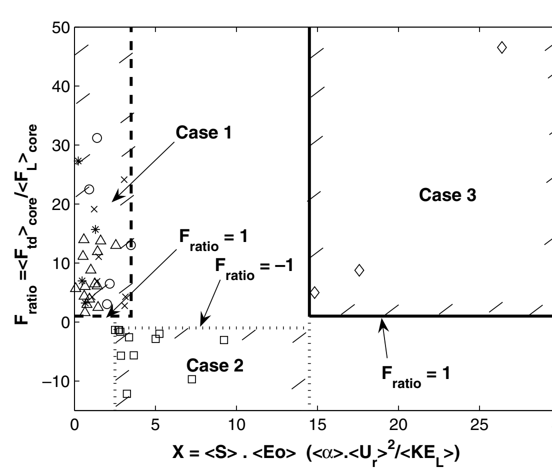

Fig. 15. The variation of F_{ratio} with X for [$*$ Michiyoshi and Serizawa (1986) data: wall-peak (case 1), × Wang et al. (1987) data: wall-peak (case 1), △ Liu (1989) data: wall-peak (case 1), ○ present data: wall-peak (case 1), □ present data: core-peak (case 2), and ◇ present data: core-peak (case 3)].

Table 2
The X parameter values for the data of Nakoryakov et al. (1996) and Ohnuki and Akimoto (2000)

Author (D_{pipe})	J_f (m/s)	J_g (m/s)	Injector type	$\langle D_b \rangle$ (mm)	$\langle \alpha \rangle$ (%)	Void fraction shape	X
Nakoryakov et al. (1996) (14.8 mm)	0.44	0.05	Cylindrical with 18 holes of 0.15 mm diameter on its circumference	2	6.9	Wall-peak	0.286
Nakoryakov et al. (1996) (14.8 mm)	0.44	0.11	Cylindrical with 18 holes of 0.15 mm diameter on its circumference	2.4	12.8	Wall-peak	0.554
Nakoryakov et al. (1996) (14.8 mm)	0.44	0.05	6 Hypodermic needles of 0.4 mm diameter	3.7	5.5	Core-peak	3.4
Nakoryakov et al. (1996) (14.8 mm)	0.44	0.11	6 Hypodermic needles of 0.4 mm diameter	3.6	11.8	Core-peak	3.3
Ohnuki and Akimoto (2000) (200 mm)	1.06	0.11	12 Porous sinter tubes of 30 mm diameter and 40 μm grain size	3.43	7.36	Wall-peak	0.245

X less than about 2.5, which results in an interfacial force balance that gives a wall-peak void profile. In larger diameter pipes, a similar distinct bubbly flow regime can be obtained with a higher range of $\langle D_b \rangle$, and consequently a higher value of X. As X increases beyond 2.5, core-peak void profiles are observed. Increasing X to greater than 14.5, causes the core-peak profiles to be more distinct (case 3), as shown by the three data points corresponding to J_f–J_g of 0.2–0.085, 0.2–0.1, and 0.26–0.1 m/s in Fig. 2a–b. There is an overlap between cases 1 and 2 for X in the range of about 2.5–3.5, where the shape of the void fraction profile will be dependant on the value of F_{ratio} as well as X. The sensitivity of the value of C_p on the relation between X and F_{ratio} was examined by varying C_p from 0.75 to 1.25. Increasing C_p in this range resulted in an increase in the value of F_{ratio} by about 160% and 68% for cases 1 and 3, and a decrease by about 50% for case 2. However, the location of the boundaries between the different cases on the map were unaffected by the value of C_p.

The above map was also checked against the data of Nakoryakov et al. (1996) and Ohnuki and Akimoto (2000) for bubbly flow in a 14.8 and 200 mm diameter pipe, respectively. For the data of Ohnuki and Akimoto (2000), the void fraction profile was wall-peak, while for the (Nakoryakov et al., 1996) data the void fraction profile changed from wall to core peak when the injector type was changed to obtain larger bubble diameters. For these data v and w are assumed equal to u and the area averaged slip ratio for Nakoryakov et al. (1996) was estimated as

$$\langle S \rangle = \frac{J_g}{J_f}\left(\frac{1}{\langle \alpha \rangle} - 1\right) \quad (23)$$

because no measurements for the bubble velocity were provided.

The flow conditions and the corresponding range of X are given in Table 2. For the wall-peak cases, the bubble diameter was relatively small and X was less than 2.5 in both the small and large diameter pipes. In the small diameter pipe, when the value of X was increased above to 3.3 by injecting larger bubbles, the void fraction profile had a core peak. This is consistent with the map shown in Fig. 15.

4. Conclusions

Experiments were performed in a 200 mm diameter vertical pipe to investigate the liquid turbulence structure of an upward fully developed two-phase bubbly flow using air and water. The measurements were performed at L/D_{pipe} of 42 at six liquid superficial velocities in the range 0.2–0.68 m/s. At each liquid superficial velocity, the gas superficial velocity was varied in the range 0.005–0.18 m/s, corresponding to an area averaged void fraction of 1.2% to 15.4% and bubble diameter in the range of 3-6 mm. The bubble characteristics were measured using a dual optical probe while the liquid turbulence characteristics were measured using single and cross hot-film anemometry.

A core-peak void fraction distribution was obtained for most flow conditions, except at low void fraction flows ($\langle \alpha \rangle \lesssim 4\%$) where a wall-peak was observed. The wall-peak profiles were associated with an increase in the bubble diameter towards the pipe wall, while for core-peak profiles the bubble diameter decreased as the pipe wall was approached. The profiles of the bubble frequency were found, in general, to follow the same trend of the void fraction profiles. The average liquid velocity profiles were more uniform than the corresponding single phase profiles for the case of a wall-peak void fraction profile. When the void profile had a core peak, the average liquid velocity in the central region was higher than the corresponding single phase profiles. In general, there is an increase in the turbulence intensity when the bubbles are introduced into the flow. However, a turbulence suppression was observed close to the wall at very low void fraction flows ($\langle \alpha \rangle \lesssim 1.6\%$). The distribution of the net radial interfacial force on the bubbles was estimated from the two-fluid model using the current measurements. The radial direction of the bubble migration in the pipe core was related to the balance between the turbulent dispersion and the lift forces. The ratio between these forces was characterized by a dimensionless group (X) that includes the area averaged Eötvös number, slip ratio, and the ratio between the apparent added kinetic energy to the liquid to the actual amount. A flow map was proposed to specify the flow conditions under which wall or core peak void distribution would occur. The data from the current measurements and existing data in small diameter was found to be in good agreement with this flow map.

References

Antal, S.P., Lahey Jr., R.T., Flaherty, J.E., 1991. Analysis of phase distribution in fully developed laminar bubbly two-phase flow. Int. J. Multiphase Flow 7, 635–652.

Beyerlein, S.W., Rainer, K.C., Horst, J.R., 1985. Prediction of bubble concentration profiles in vertical turbulent two-phase flow. Int. J. Multiphase Flow 11, 629–641.

Browne, L., Antonia, R.A., Chua, L., 1989. Calibration of x-probes for turbulent flow measurements. Exp. Fluids 3, 201–208.

Cheng, H., Hills, J.H., Azzopradi, B.J., 1998. A study of the bubble-to-slug transition in the vertical gas–liquid flow in columns of different diameter. Int. J. Multiphase Flow 24, 431–452.

Clift, R., Grace, J.R., Weber, M.E., 1978. Bubbles, Drops and Particles. Academic Press, New York.

Ervin, E.A., Tryggvason, G., 1997. The rise of bubbles in a vertical shear flow. J. Fluids Eng. 119, 443–449.

Esmaeeli, A., Ervin, E., Tryggvason, G., 1994. Numerical Simulations of Rising Bubbles in Bubbles Dynamics and Interface Phenomena. Kluwer Academic, Dordrecht.

Farrar, B., Samways, A., Ali, J., Bruun, H., 1995. A computer-based hot-film technique for two-phase flow measurements. Meas. Sci. Technol. 6, 1528–1537.

Herringe, R.A., Davis, M.R., 1976. Structural development of gas–liquid mixture flows. J. Fluid Mech. 73, 97–123.

Hibiki, T., Ishii, M., 1999. Experimental study on interfacial area transport in bubbly two-phase flows. Int. J. Heat Mass Transfer 42, 3019–3035.

Kariyasaki, A., 1987. Behavior of single gas bubble in a liquid flow with linear velocity profile. ASME Therm. Eng. Joint Conf., 261.

Lahey Jr., R.T., Lopez de Bertodano, M., Jones Jr., O.C., 1993. Phase distribution in complex geometry conduits. Nucl. Eng. Des. 141, 177–201.

Laufer, J., 1954. The structure of turbulent in fully developed pipe flow. NACA, 1174.

Lawn, C.J., 1971. The determination of the rate of dissipation in the turbulent pipe flow. J. Fluid Mech. 48, 477–505.

Liu, T.J., 1989. Turbulence modeling in bubbly two-phase flows. Ph.D. Thesis, Northwestern University.

Liu, T.J., 2002. An effective signal processing method for resistivity probe measurements in a two-phase bubbly flow. Meas. Sci. Technol. 13, 206–217.

Liu, T.J., Bankoff, S.G., 1993a. Structure of air–water bubbly flow in a vertical pipe – i. Int. J. Heat Mass Transfer 36, 1049–1060.

Liu, T.J., Bankoff, S.G., 1993b. Structure of air–water bubbly flow in a vertical pipe – ii. Int. J. Heat Mass Transfer 36, 1061–1072.

Lopez de Bertodano, M., Lahey Jr., R.T., Jones, O.C., 1994. Phase distribution in bubbly two-phase flow in vertical ducts. Int. J. Multiphase Flow 20, 805–818.

Lopez de Bertodano, M., Moraga, F.J., Drew, D.A., Lahey Jr., R.T., 2004. The modeling of lift and dispersion forces in two-phase model simulations of a bubbly jet. J. Fluids Eng. 126, 573–577.

Michiyoshi, I., Serizawa, A., 1986. Turbulence in two-phase bubble flow. Nucl. Eng. Des. 95, 253–267.

Nakoryakov, V.E., Kashinsky, O., Randin, V., Timkin, L., 1996. Gas–liquid bubbly flow in vertical pipes. J. Fluids Eng. 118, 377–382.

Ohnuki, A., Akimoto, H., 2000. Experimental study on transition of flow pattern and phase distribution in upward air–water two-phase flow along a large vertical pipe. Int. J. Multiphase Flow 26, 367–386.

Ohnuki, A., Akimoto, H., 2001. Model development for bubble turbulent diffusion and bubble diameter in large vertical pipes. J. Nucl. Sci. Technol. 38, 1074–7080.

Prasser, H.M., Beyer, M., Bottger, A., Carl, H., Lucas, D., Schaffrath, A., Schutz, P., Weiss, F.P., Zschau, J., 2005. Influence of the pipe diameter on the structure of the gas–liquid interface in a vertical two-phase pipe flow. Nucl. Technol. 152, 3–22.

Revankar, S., Ishii, M., 1992. Local interfacial area measurement in bubbly flow. Int. J. Heat Mass Transfer 35, 913–925.

Sato, Y., Sekoguchi, K., 1975. Liquid velocity distribution in two-phase bubble flow. Int. J. Multiphase Flow 2, 79–95.

Schlichting, H., 1979. Boundary Layer Theory. McGraw Hill, NewYork.

Serizawa, A., Kataoka, I., Mischiyoshi, I., 1975. Turbulence structure of air–water bubbly flow – ii. Int. J. Multiphase Flow 2, 235–246.

Shawkat, M.E., 2007. Liquid turbulence structure in two-phase bubbly flow in a large diameter vertical pipe. Ph.D. Thesis, McMaster University.

Shawkat, M.E., Ching, C.Y., Shoukri, M., 2007. On the liquid turbulence energy spectra in two-phase bubbly flow in a large diameter vertical pipe. Int. J. Multiphase Flow 33, 300–316.

Shen, X., Mishima, K., Nakamura, H., 2005. Two-phase flow distribution in a vertical large diameter pipe. Int. J. Heat Mass Transfer 48, 211–225.

Shoukri, M., Hassan, I., Gerges, I., 2003. Two phase bubbly flow structure in large diameter vertical pipe. Can. J. Chem. Eng. 18, 205–211.

Theofanous, T.G., Sullivan, J., 1982. Turbulence in two-phase dispersed flows. J. Fluid Mech. 116, 343–362.

Tomiyama, A., Tamai, H., Zun, I., Hosokawa, S., 2002. Transverse migration of single bubbles in simple shear flows. Chem. Eng. Sci. 57, 1849–1858.

Troshko, A., Hassan, Y., 2001. A two-equation turbulence model of turbulent bubbly flows. Int. J. Multiphase flow 27, 1965–2000.

Uga, T., 1972. Determination of bubble-size distribution in BWR. Nucl. Eng. Des. 22, 252–261.

Wang, G., Ching, C.Y., 2001. Measurement of multiple gas-bubble velocities in gas–liquid flows using hot-film anemometry. Exper. Fluids 31, 428–439.

Wang, S.K., Lee, S.J., Jones Jr., O.C., Lahey Jr., R.T., 1987. 3-d turbulence structure and phase distribution measurements in bubbly two-phase flows. Int. J. Multiphase Flow 13, 327–343.

Yavuzkurt, S., 1984. A guide to uncertainty analysis of hot-wire data. J. Fluids Eng. 106, 181–186.

Yoneda, K., Yasuo, A., Okawa, T., 2002. Flow structure and bubble characteristics of steamwater two-phase flow in a large-diameter pipe. Nucl. Eng. Des. 217, 267–281.

Zun, I., 1988. Transition from Wall Void Peaking to Core Void Peaking in Turbulent Bubbly Flow. In: Transient Phenomena in Multiphase Flow. Hemisphere Publishing Incorp.